

Renan Cavenaghi Silva<sup>1</sup> & Douglas D. Bueno<sup>2</sup>

<sup>1,2</sup> São Paulo State University (UNESP), School of Engineering, Ilha Solteira 15385-000, SP, Brazil Department of Mechanical Engineering. cavenaghi.silva@unesp.br
<sup>2</sup>Department of Mechanical Engineering. douglas.bueno@unesp.br

#### **Abstract**

An intriguing feature observed during the flight of feathered animals is the formation of gaps between feathers during the upstroke. These ventilation gaps offer an alternative path with less resistance for air to flow through, reducing the influence of forces opposing the motion. These channels close during the downstroke, allowing the wing to provide the required aerodynamic forces. We describe a mechanism to open these channels for feathers located in the innermost sections of the wing based on the inertial loads imposed by the flapping motion, which increases along the wing-span and allows the distal feathers to deflect more than its adjacent proximal feather. This effect occurs only in one direction, as in the opposite direction the deflection is limited by the contact forces in the overlap region. This mechanism requires modeling the feathers as flexible structural members. Therefore, we develop a model for the flexible feather from a flapping-wing to investigate the formation of ventilation gaps based on the Absolute Nodal Coordinate Formulation, which is a multi-body approach suited for the analysis of structures subjected to large displacements and deflections.

Keywords: FWUAV; Ventilation; Multi-Body Dynamics; Absolute Nodal Coordinate Formulation; Contact.

## 1. Introduction

Competition in nature resulted in the development by some species of the ability to sustain powered flight. This form of locomotion allows flying animals to spot prey from privileged positions, escape from predators, build nests in safe locations, and migrate for foraging food. Unlike man-made aircraft, which typically use propellers to provide thrust, insects and avians flap their wings to provide both the lift and thrust required to fly. Although flapping can be perceived as more energetically demanding than a fixed-wing configuration, [1] finds that an optimal flapping pattern on an insect scale is 27% more efficient than an optimized fixed wing by exploiting the unsteady aerodynamic effects during wing reversal. In addition, the absence of fast-rotating propellers makes flapping-wing vehicles suitable for applications involving human-vehicle interaction.

A characteristic that distinguishes avians from other flying animals is that their entire body is covered by feathers, providing thermal insulation, directional air permeability [2], and damage tolerance [3]. Wing feathers are composed of hierarchical structures ranging from the micro to the macroscopic scales that complement their highly optimized muscular and skeletal system allowing the bird to morph their wings and adapt to the flying regime for maximum performance [4, 5], resulting in a great biodiversity of avian species specializing in different aspects of flight such as speed, maneuverability, noise, and range [6].

The scale of birds is limited by biological factors, such as the power that can be developed through muscles and material limitations to withstand inertial and aerodynamic loads. The largest species, such as the snowy albatross (*Diomedea exulans*), can reach a wingspan of 3.5m, while the heaviest species, such as the kori bustard (*Ardeotis kori*), can weigh up to 18kg. Therefore, understanding the fundamentals of the biological design of natural flyers may aid in the development of engineering solutions to address common problems in the aeronautic industry (e.g., stability, efficiency, performance, noise and comfort).

An interesting phenomenon observed in feathered avians is the formation of gaps that allow air to ventilate between feathers during the upstroke. These gaps close during the downstroke, forming a smooth and

impermeable wing surface to provide the required lift and thrust to maintain flight. This ventilation effect is likely to decrease adverse aerodynamic loads during the upstroke, resulting in an increase in net lift and thrust forces from the flapping cycle. [7] attribute the formation of gaps to an aeroelastic interaction of the asymmetric primary feathers that align with the resultant flow. However, gaps can also be observed between secondary feathers located in the inner sections of the wings, which are symmetric and parallel to the airflow. On an insect scale, [8] show that the deformation of the wing structure is dominated by inertial forces, suggesting that a simpler analysis framework based on the structural response of the wing may give accurate results regarding the geometry of the ventilation channels. Therefore, we investigate a mechanism for the secondaries based on the structural response of the feathers to the imposed flapping motion.

The remaining part of this work is organized as follows: Section (2). describes the problem under investigation. Section (3). presents the kinematics of the flapping-wing. Section (4). we discuss a mechanism for the formation of ventilation channels across the secondary feathers. Section (5). present the modeling of the flexible feather using the ANCF. Section 6 presents the numerical solution of the trajectories of the feathered flapping-wing model. Section (7). presents the final-remarks.

## 2. Methodology

The problem addressed herein is the ventilation mechanism observed in the flight feathers (feathers attached to the wing) of avians, illustrated in Figures 1a and 1b by two snapshots indicating the state of the ventilation channels between feathers. During the upstroke (Figure 1a), the gaps between the feathers form ventilation channels that allow air to flow easily through. In the downstroke phase (Figure 1b), these channels close and the feathers on the wing form a smooth and impermeable surface to capture air. This feature reduces aerodynamic loads during the upstroke phase, when the direction of these loads adversely influences the generation of lift and thrust forces.

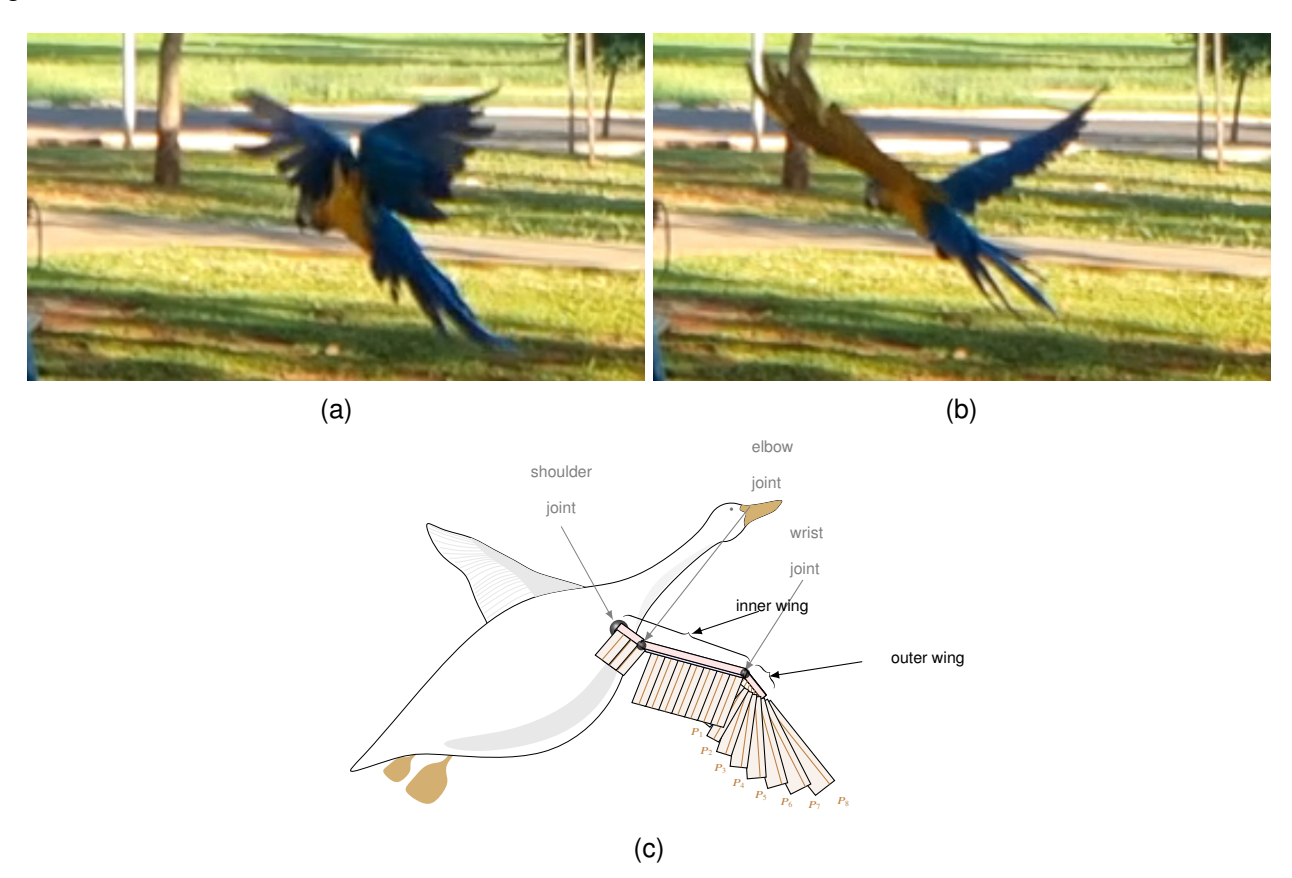


Figure 1 – Snapshots from an avian (*Ara araraura*) during its flight. During the upstroke (a) gaps between feather are observed, and during downstroke (b) they closes. (c) schematic from the feathered wing.

The feathered wing is described according to the schematic in Figure 1c. The wing is divided into inner and outer wings, representing the stiff avian bones. One end of the inner-wing is constrained to the avian body

by means of a spherical joint, which allows the wing to rotate with respect to any axis, similarly to the human shoulder joint. The inner wing is subdivided into a short humerus and a long ulna by means of an additional rotational joint, allowing for folding and extension motions, analogous to an elbow joint. The outer wing is constrained to the other end of the inner wing by means of a spherical joint, which functions as the wrist joint. The wings are covered by feathers that, in addition to their biological functions, constitute the airfoil shape of the wing. The feathers are composed of two parts: a central shaft denoted by the rachis and the vanes. The rachis is the main structural element and is attached to the bone in a cantilevered configuration. The feather vanes are composed of numerous microscopic hierarchical structures attached transversely along the rachis, forming a tightly woven mesh that captures air and can disassemble in the occurrence of large localized loads.

The feathers attached to the outer wing are denoted as primary feathers  $P_i$ ,  $i=1,\ldots n_P$ , with  $n_P$  being the number of primary feathers. The primaries have asymmetric vanes, with a narrow leading-edge and a broader trailing-edge, and are attached to the bone at a varying angle that extends further than the bone. The secondaries,  $S_i$ ,  $i=1,\ldots n_S$ , with  $n_S$  being the number of secondary feathers, have symmetric vanes and are attached to the inner wing perpendicular to the bone axis. The feathers are located such that the leading-edge vane of the proximal feather overlaps the trailing-edge of the distal feather [9]. This overlap allows for the morphing feature and plays a crucial role to close the ventilation gaps between the secondaries during the downstroke.

A mechanism to explain the formation of ventilation channels in the outer wing is the aeroelastic divergence of the asymmetric primaries [7], which aligns the primary feathers with the incident airflow. However, we can also observe the separation of the secondary feathers during the upstroke, which are symmetric and attached parallel to the airflow. On the other hand, the flapping pattern generates inertial forces that can be tailored to separate the feathers, thus creating the ventilation gaps.

# 3. Flapping-Wing Kinematics

The model consists of a rigid inner wing whose motion is a prescribed function of time. Attached to it are flexible structures representing the feathers, which are collocated so that the vanes overlap. The imposed motion accelerates every point of the feather, resulting in inertial loads that are balanced by a corresponding elastic restoring force.

The flapping pattern is parameterized by a combination of two rotations: a flapping rotation in the y direction and a pitch rotation in the new  $_{\mathscr{B}_1}x$  direction. An additional rotation with respect to the  $_{\mathscr{B}_2}z$  axis parameterizes the attachment angle  $\alpha_G$  of the feather. An angle of  $\alpha_G = -\frac{\pi}{2}$  represents a feather attached perpendicular to the bone axis, whereas a value of zero represents the feathers parallel. The secondary feathers are attached perpendicularly, whereas the primaries transition from perpendicular to parallel. The rotation matrices that transform a vector between different coordinate systems are defined as follows.

$$\boldsymbol{T}_{\alpha_{F}} = \begin{bmatrix} \cos\left(\alpha_{F}\right) & 0 & -\sin\left(\alpha_{F}\right) \\ 0 & 1 & 0 \\ \sin\left(\alpha_{F}\right) & 0 & \cos\left(\alpha_{F}\right) \end{bmatrix}, \ \boldsymbol{T}_{\alpha_{T}} = \begin{bmatrix} 1 & 0 & 0 \\ 0 & \cos\left(\alpha_{T}\right) & \sin\left(\alpha_{T}\right) \\ 0 & -\sin\left(\alpha_{T}\right) & \cos\left(\alpha_{T}\right) \end{bmatrix}, \ \boldsymbol{T}_{\alpha_{G}} = \begin{bmatrix} \cos\left(\alpha_{G}\right) & \sin\left(\alpha_{G}\right) & 0 \\ -\sin\left(\alpha_{G}\right) & \cos\left(\alpha_{G}\right) & 0 \\ 0 & 0 & 1 \end{bmatrix}, \ (1)$$

where  $T_{\alpha_F}$ ,  $T_{\alpha_T}$ , and  $T_{\alpha_G}$  denotes the flapping, pitch, and attachment angle rotations, respectively. Two points, P and F, are defined. Point P corresponds to the position of the feather attachment point with respect to the wing bone, and point F corresponds to an arbitrary point along the longitudinal axis of the feather. The positions of these points are parameterized in their local coordinate systems as follows:

$$\mathcal{B}_1 \boldsymbol{r}_P = \begin{cases} l_p \\ 0 \\ 0 \end{cases}, \quad \mathcal{B}_3 \boldsymbol{r}_F = \begin{cases} e_y \\ 0 \\ 0 \end{cases}, \tag{2}$$

where  $l_p$  is the distance from the feather to the flapping joint, and  $e_y$  the distance from the point F to its attachment to the bone. The points and rotations are illustrated in Figure 2.

The position of the points P and F is transformed to the inertial coordinate system through the following equations.

$$\mathbf{r}_{P}(t) = \mathbf{T}_{\alpha_{F}}^{\top}(t)_{\mathscr{B}_{1}} \mathbf{r}_{P} \tag{3}$$

$$\boldsymbol{r}_{F}(t) = \boldsymbol{T}_{\alpha_{F}}^{\top}(t) \left( \boldsymbol{\beta}_{1} \boldsymbol{r}_{P} + \boldsymbol{T}_{\alpha_{T}}^{\top}(t) \boldsymbol{\beta}_{2} \boldsymbol{r}_{F} \right), \tag{4}$$

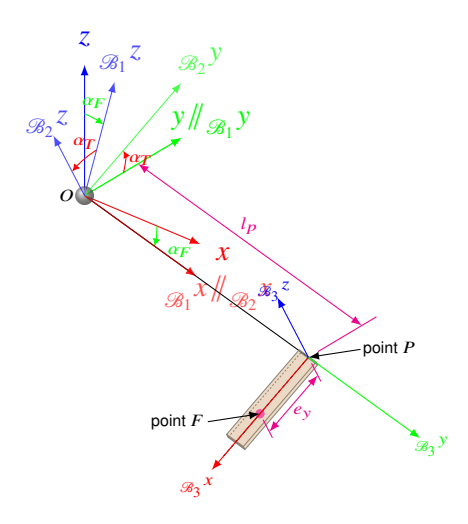


Figure 2 – Kinematics of the feather.

The velocity of the points P and F is obtained by differentiating Equations (3) and (4) with respect to the time t:

$$\dot{\boldsymbol{r}}_{P}(t) = \dot{\boldsymbol{T}}_{\alpha_{F}}^{\top}(t)_{\mathscr{B}_{1}} \boldsymbol{r}_{P},\tag{5}$$

$$\dot{\mathbf{r}}_{F}(t) = \dot{\mathbf{T}}_{\alpha_{F}}^{\top}(t) \left( \mathbf{g}_{1} \mathbf{r}_{P} + \mathbf{T}_{\alpha_{T}}^{\top}(t) \mathbf{g}_{2} \mathbf{r}_{F} \right) + \mathbf{T}_{\alpha_{F}}^{\top}(t) \dot{\mathbf{T}}_{\alpha_{T}}^{\top}(t) \mathbf{g}_{2} \mathbf{r}_{F}, \tag{6}$$

and acceleration at points P and F are obtained by differentiating Equations (5) and (6) with respect to time:

$$\ddot{\boldsymbol{r}}_{P}(t) = \ddot{\boldsymbol{T}}_{\alpha_{F}}^{\top}(t)_{\mathscr{B}_{1}} \boldsymbol{r}_{P},\tag{7}$$

$$\ddot{\boldsymbol{r}}_{F}(t) = \ddot{\boldsymbol{T}}_{\alpha_{F}}^{\top}(t) \left( \boldsymbol{\beta}_{1} \boldsymbol{r}_{P} + \boldsymbol{T}_{\alpha_{T}}^{\top}(t) \boldsymbol{\beta}_{2} \boldsymbol{r}_{F} \right) + 2 \dot{\boldsymbol{T}}_{\alpha_{F}}^{\top}(t) \dot{\boldsymbol{T}}_{\alpha_{T}}^{\top}(t) \boldsymbol{\beta}_{2} \boldsymbol{r}_{F} + \boldsymbol{T}_{\alpha_{F}}^{\top} \ddot{\boldsymbol{T}}_{\alpha_{T}}^{\top} \boldsymbol{\beta}_{2} \boldsymbol{r}_{F}. \tag{8}$$

For the ventilation to be effective, it is necessary to open the channels during the upstroke and close them during the downstroke. According to the rotation matrices and the coordinate system employed for the model, the downstroke is defined when the angular velocity of the flapping motion is positive, i.e.,  $\dot{\alpha}_F > 0$ . Consider the pair of feathers illustrated in the scheme shown in Figure 3. The proximal feather is positioned in the wing so that its leading-edge vane overlaps the trailing-edge of the distal feather. The inertial loads acting on each feather due to the imposed flapping motion are illustrated in Figure 3a. The load on the distal feather is represented by a larger distribution since it is located further from the rotation axis, allowing the distal feather to deflect more than the proximal feather in the negative vertical direction, i.e.,  $(-\frac{1}{3}z)$ , as shown in Figure 3b.

In the positive direction  $(+_{\mathscr{B}_3}\mathcal{I})$ , the deflection of the distal feather conforms to the deflection of the proximal feather due to the overlap, which restricts additional deformation, as represented in Figure 3c.

Thus, the deflection must occur in the downward direction to open the ventilation channels during the upstroke. During the downstroke, the distal feather should be pushed against the proximal feather to create a smooth and closed wing. To maintain this effect throughout the flapping cycle, the acceleration along the feather should oppose the velocity of the attachment point.

The velocity of a flapping-only motion lags the acceleration by  $\pi/2$  radians, as illustrated in Figure 4 for a sinusoidal signal with unitary frequency and amplitude. Thus, the conditions for opening the ventilation channels are favorable for half of the flapping cycle, resulting in the adverse effect of opening the ventilation channels during half of the downstroke. Thus, we search for a combination of a flapping and pitch rotations such that the resulting linear acceleration of a point along the feather is opposing the velocity of its corresponding attachment point.

The velocity of point P and the acceleration of point F are mapped to the coordinate system  $\mathcal{B}_1$  using the transformation matrices of Equation (1), resulting in the following expressions:

$$\mathcal{B}_{1}\dot{\boldsymbol{r}}_{P}(t) = \begin{bmatrix} \cos\left(\alpha_{F}(t)\right) & 0 & -\sin\left(\alpha_{F}(t)\right) \\ 0 & 1 & 0 \\ \sin\left(\alpha_{F}(t)\right) & 0 & \cos\left(\alpha_{F}(t)\right) \end{bmatrix} \begin{cases} -l_{p}\sin(\alpha_{F}(t))\dot{\alpha}_{F}(t) \\ 0 \\ -l_{p}\cos(\alpha_{F}(t))\dot{\alpha}_{F}(t) \end{cases} = \begin{cases} 0 \\ 0 \\ -l_{p}\dot{\alpha}_{F}(t), \end{cases}$$
(9)

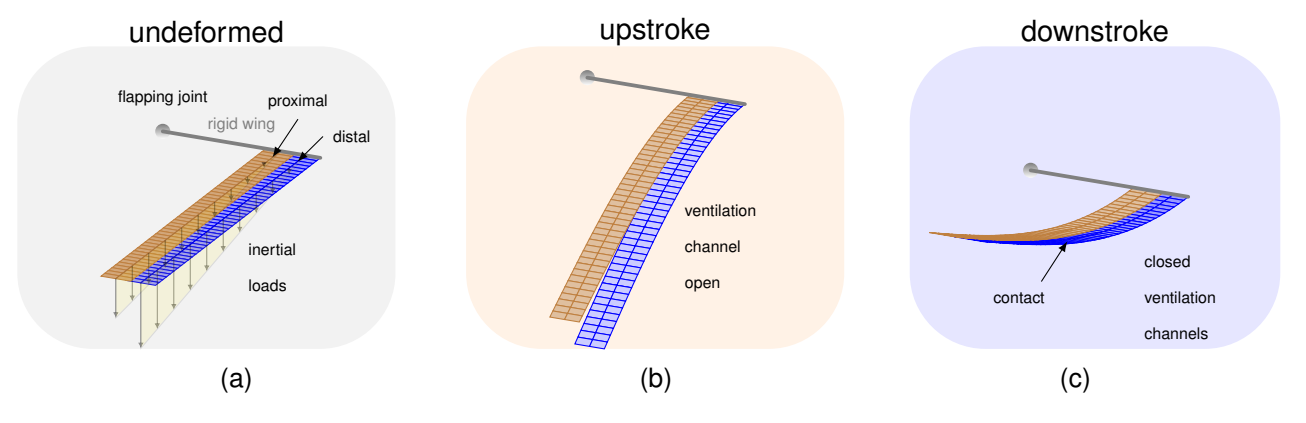


Figure 3 – Scheme of formation of the ventilation channels. (a) shows the undeformed feathers and the inertial loads. (b) shows the upstroke, where the feathers deform to balance their inertial loads. (c) shows the feathers deformed in the downstroke. Note the contact limiting the deflection of the distal feather.

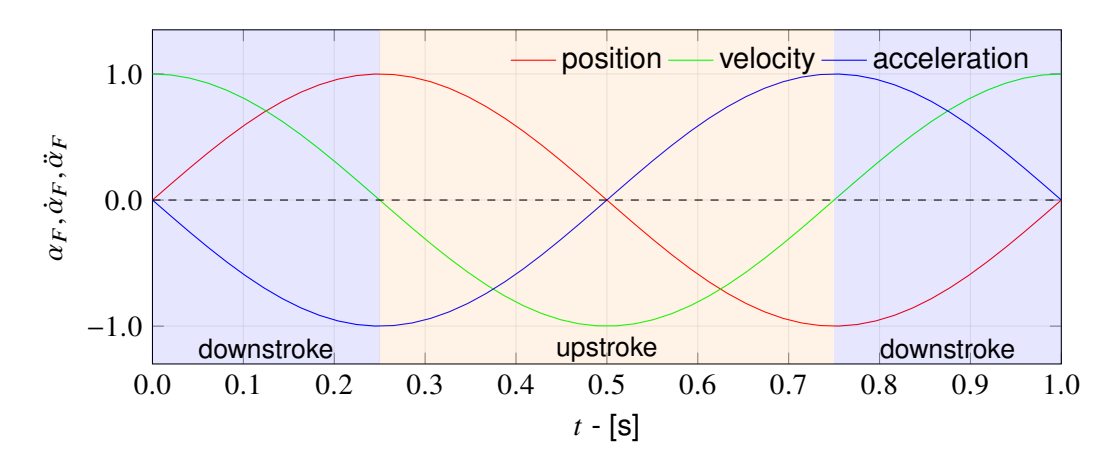


Figure 4 – Velocity and acceleration of a sinusoidal signal. The acceleration is opposing the velocity during half of the cycle.

$$\mathcal{B}_{1}\ddot{\boldsymbol{r}}_{F}(t) = \begin{cases}
-e_{y}\sin(\alpha_{T}(t))\ddot{\alpha}_{F}(t) - 2e_{y}\cos(\alpha_{T}(t))\dot{\alpha}_{F}(t)\dot{\alpha}_{T}(t) - l_{p}\left(\dot{\alpha}_{F}(t)\right)^{2} \\
e_{y}\left(\sin(\alpha_{T}(t))\ddot{\alpha}_{T}(t) + \cos(\alpha_{T}(t))\left(\dot{\alpha}_{T}(t)\right)^{2}\right) \\
e_{y}\sin(\alpha_{T}(t))\left(\dot{\alpha}_{F}(t)\right)^{2} + e_{y}\sin(\alpha_{T}(t))\left(\dot{\alpha}_{T}(t)\right)^{2} - e_{y}\cos(\alpha_{T}(t))\ddot{\alpha}_{T}(t) - l_{p}\ddot{\alpha}_{F}(t)
\end{cases}.$$
(10)

The vertical component of the velocity from the feather attachment point and the vertical component of the acceleration from point F with respect to  $\mathcal{B}_1$  are:

$$_{\mathcal{B}_{1}}\dot{\boldsymbol{r}}_{P}\cdot_{\mathcal{B}_{1}}e_{k}=l_{p}\dot{\alpha}_{F}(t). \tag{11}$$

$$_{\mathcal{B}_1}\ddot{\boldsymbol{r}}_F \cdot _{\mathcal{B}_1} e_k = e_y \sin \left(\alpha_T(t)\right) \left(\dot{\alpha}_F(t)\right)^2 + e_y \sin \left(\alpha_T(t)\right) \left(\dot{\alpha}_T(t)\right)^2 - e_y \cos \left(\alpha_T(t)\right) \ddot{\alpha}_T(t) - l_p \ddot{\alpha}_F(t), \tag{12}$$

The acceleration of the feather opposes the tangential velocity of the attachment point if their product is negative. Thus, the following kinematic ventilation parameter is defined:

$$k_{v} = \operatorname{sign}\left(-l_{p}\dot{\alpha}_{F}\left(e_{y}s_{\alpha_{T}}\dot{\alpha}_{F}^{2} + e_{y}s_{\alpha_{T}}\dot{\alpha}_{T}^{2} - e_{y}c_{\alpha_{T}}\ddot{\alpha}_{T} - l_{p}\ddot{\alpha}_{F}\right)\right),\tag{13}$$

which evaluates to:

$$k_{v} = \begin{cases} +1, & \text{if opposite direction,} \\ -1, & \text{otherwise.} \end{cases}$$
 (14)

The kinematic ventilation parameter provides a simplified measure to determine whether a given flapping pattern enhances the ventilation effect. Since this parameter is derived from the system's kinematics, its computational cost is negligible compared to solving the trajectories of the flexible feather model.

## 4. Formation from the Ventilation Gaps

The mechanism for opening the ventilation channels is described by the structural dynamics of the flexible feathers. Consider a pair of overlapping structures, denoted by  $S_1$  and  $S_2$ , representing the proximal and distal feathers, respectively. The overlap  $w_o$  is defined as:

$$w_o = 1 - \frac{h_s}{w},\tag{15}$$

with  $h_s$  being the spacing between the feathers and w the width of the feather. A value of  $w_o = 0$  denotes no overlap and  $w_o = 1$  denotes complete overlap. The feather  $S_1$  is attached to the wing at a distance  $l_p$  from the origin. Thus, the feather  $S_2$  is attached to the wing at position  $(l_p + (1 - w_o)w)$ .

The difference between adjacent feathers in Equation (12) is due to the tangential acceleration induced by the flapping motion. This is given by the last term of the expression, which evaluates for the proximal feather as follows:

$$a_T^{(1)} = -l_p \ddot{\alpha}_F(t),$$
 (16)

and for the distal feather

$$a_T^{(2)} = -(l_p + (1 - w_o)w)\ddot{\alpha}_F(t). \tag{17}$$

By dividing Equation (17) by Equation (16), we define the following amplification ratio  $R_{dta}$ .

$$R_{dta} = 1 + \frac{(1 - w_o)w}{l_p}. (18)$$

Equation (18) is illustrated in Figure 5 for various attachment positions  $l_p$  along the wing. Note that the amplification is more significant for low values of  $l_p$ , which is the case for the secondary feathers, attached to the inner-most sections of the wing. We suspect that this difference is enough to open the ventilation

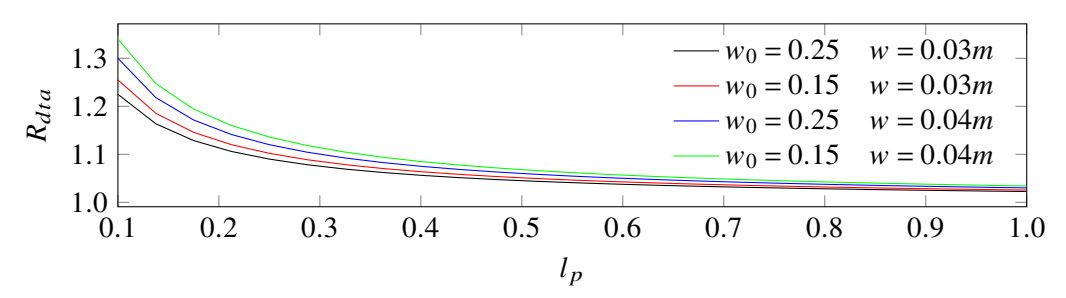


Figure 5 – Kinematic amplification of the acceleration induced by the flapping motion in a distal feather.

channels or at least initiate the process if this phenomenon is dominated by aeroelastic effects. Consider the following reasoning: the inertial loads caused by the flapping motion acting on a flexible feather attached at  $l_p$  result in a certain deflection. For the distal feather located at  $l_p + (1 - w_o)w$ , the inertial loads increase due to the feather being attached farther from the flapping origin and are balanced by a corresponding increase in deflection. This differential deflection creates gaps that provide an alternative path for air to flow in the innermost sections of the wing. The size of these gaps can be further amplified if the flapping frequency is close to the natural frequency of the first bending mode.

## 5. Flexible Feather Dynamics

The feather is discretized using three-dimensional beam elements from the absolute nodal coordinate formulation (ANCF). This approach is suitable for modeling structures subject to large displacements and deflections [10]. The position, velocity and acceleration of an arbitrary particle in the *i*th ANCF beam element are defined as, respectively:

$$\mathbf{r}(t,\mathbf{x}) = \mathbf{S}(\xi,\eta,\zeta)\mathbf{e}(t),\tag{19}$$

$$\dot{\mathbf{r}}(t,\mathbf{x}) = \mathbf{S}(\xi,\eta,\zeta)\dot{\mathbf{e}}(t),\tag{20}$$

$$\ddot{\mathbf{r}}(t,\mathbf{x}) = \mathbf{S}(\xi,\eta,\zeta)\ddot{\mathbf{e}}(t),\tag{21}$$

where the position of the particle in the local coordinate system,  $x = \{x, y, z\}$  is normalized with respect to the element length  $l_e$  by

$$\xi = \frac{x}{l_e}, \quad \eta = \frac{y}{l_e}, \quad \zeta = \frac{z}{l_e}. \tag{22}$$

The shape function of the three-dimensional beam element is defined by [11] as:

$$S(\xi, \eta, \zeta) = [s_1 I, s_2 I, s_3 I, s_4 I, s_5 I, s_6 I, s_7 I, s_8 I],$$
(23)

where I is the identity matrix, with dimension  $3 \times 3$ , and  $s_i$ , i = 1, ..., 8 are the coefficients of the shape function. The coefficients and derivatives with respect to the local coordinate system are presented in Table 1.

Table 1 – Shape function of the low-order beam element and derivatives with respect to the local coordinate system.

	$s_i$	$\frac{\partial s_i}{\partial \xi} \frac{\partial \xi}{x}$	$\frac{\partial s_i}{\partial \eta} \frac{\partial \eta}{\partial y}$	$\frac{\partial s_i}{\partial \zeta} \frac{\partial \zeta}{\partial z}$
$s_1$	$1 - 3\xi^2 + 2\xi^3$	$\frac{1}{l_{z}} \left( -6\xi + 6\xi^{2} \right)$	0	0
$s_2$	$l_e \left( \xi - 2\xi^2 + \xi^3 \right)$	$1 - 4\xi + 3\xi^2$	0	0
<i>S</i> 3	$l_e\left(\eta-\xi\eta ight)$	$-\eta$	$1-\xi$	0
<i>S</i> 4	$l_e\left(\eta - \xi\zeta\right)$	$-\zeta$	0	$1-\xi$
<i>S</i> <sub>5</sub>	$3\xi^2 - 2\xi^3$	$\frac{1}{l_a}\left(6\xi-6\xi^2\right)$	0	0
<i>s</i> <sub>6</sub>	$l_e\left(-\xi^2+\xi^3\right)$	$(-2\xi + 3\xi^2)$	0	0
<b>S</b> 7	$l_e \xi \eta$	$\eta$	ξ	0
<b>S</b> 8	$l_e \xi \zeta$	ζ	0	ξ

A limitation of the beam element used is the problem of Poisson's locking, which can lead to inaccurate results [12]. To avoid this issue, high-order polynomials can be used to parameterize transversal deformations, as in [13] or in [14]. However, using high-order elements also increases the computational time. Therefore, we set the Poisson coefficient to zero to avoid this problem.

The nodal coordinates of the ANCF three-dimensional beam element consist of the positions and slopes of the nodes A and B with respect to the absolute coordinate system, resulting in a total of 12 coordinates per node. Therefore, each element is represented by 24 nodal coordinates, as shown in the following expression:

$$e(t) = \left\{ \mathbf{r}_{A}^{\mathsf{T}} \quad \frac{\partial \mathbf{r}_{A}}{\partial x}^{\mathsf{T}} \quad \frac{\partial \mathbf{r}_{A}}{\partial y}^{\mathsf{T}} \quad \frac{\partial \mathbf{r}_{A}}{\partial z}^{\mathsf{T}} \quad \mathbf{r}_{B}^{\mathsf{T}} \quad \frac{\partial \mathbf{r}_{B}}{\partial x}^{\mathsf{T}} \quad \frac{\partial \mathbf{r}_{B}}{\partial y}^{\mathsf{T}} \quad \frac{\partial \mathbf{r}_{B}}{\partial z}^{\mathsf{T}} \right\}^{\mathsf{T}}.$$
 (24)

## 5.1 Mass Matrix

The kinetic energy of the ANCF beam element is defined by:

$$\mathcal{T} = \frac{1}{2} \int_{V_e} \rho \dot{\boldsymbol{r}}^{\top} \dot{\boldsymbol{r}} dV. \tag{25}$$

Substituting Equation 20 into Equation 25, the kinetic energy is:

$$\mathcal{T} = \frac{1}{2} \int_{V_0} \rho \dot{\boldsymbol{e}}^{\mathsf{T}} \boldsymbol{S}^{\mathsf{T}} \boldsymbol{S} \dot{\boldsymbol{e}} dV. \tag{26}$$

The nodal coordinate vector is constant within the element volume, such that it is factored out of the integral, resulting in the following expression:

$$\mathcal{T} = \frac{1}{2} \dot{\boldsymbol{e}}^{\mathsf{T}} \left[ \rho \int_{V_e} \mathbf{S}^{\mathsf{T}} \mathbf{S} dV \right] \dot{\boldsymbol{e}}, \tag{27}$$

and the term inside the bracket is the constant mass matrix:

$$\mathbf{M} = \rho \int_{V_{-}} \mathbf{S}^{\top} \mathbf{S} dV. \tag{28}$$

The coefficients for the beam element are obtained by solving the quadrature and compared with the values obtained in [15].

## 5.2 Structural Forces

The potential elastic energy is obtained from a continuum mechanics approach [16] by relating the components of the deformation gradient with the Lamé's constants defining the material properties using the following expression:

$$\mathcal{U}_{e} = \int_{V_{e}} \frac{\lambda + 2G}{2} \left( \epsilon_{11}^{2} + \epsilon_{22}^{2} + \epsilon_{33}^{2} \right) + \lambda \left( \epsilon_{11} \epsilon_{22} + \epsilon_{11} \epsilon_{33} + \epsilon_{22} \epsilon_{33} \right) + 2G \left( \epsilon_{12}^{2} + \epsilon_{13}^{2} + \epsilon_{23}^{2} \right) dV, \tag{29}$$

where the Lamé's constants are defined for an isotropic elastic material as:

$$\lambda = \frac{E\nu}{(1+\nu)(1-2\nu)}, \quad G = \frac{E}{2(1+\nu)}.$$
 (30)

The elastic force is obtained by differentiating Equation (29) with respect to the nodal coordinates:

$$f_e(\mathbf{e}(t)) = -\frac{\partial \mathcal{U}_e}{\partial \mathbf{e}}.$$
 (31)

The procedure presented by [17] using invariant matrices is used to avoid computing a numerical quadrature for each time that the elastic forces must be obtained, significantly improving the computational time. A similar procedure is used to model the damping forces [18].

## 5.3 Mesh Assembly

The feather mesh is composed of a total of n beam elements, connected such that the node of one element is the starting node of the next. This results in a total of 12(n+1) nodal coordinates per structure. Thus, the nodal coordinates of the ith feather are defined as:

$$\boldsymbol{e}^{(i)}(t) = \left\{ \left( \boldsymbol{e}_{1,A}^{(i)} \right)^{\mathsf{T}} \quad \left( \boldsymbol{e}_{2,A}^{(i)} \right)^{\mathsf{T}} \quad \dots \quad \left( \boldsymbol{e}_{n,A}^{(i)} \right)^{\mathsf{T}} \quad \left( \boldsymbol{e}_{n,B}^{(i)} \right)^{\mathsf{T}} \right\}^{\mathsf{T}}. \tag{32}$$

# 5.4 Flapping Motion

The flapping pattern is defined according to [1]. The smooth triangular function is used to parameterize the flapping motion:

$$\alpha_F(t) = \frac{a_F}{\sin^{-1}(K)} \sin^{-1}(K \sin(\omega_F t)), \tag{33}$$

where  $a_F$  is the flapping amplitude,  $\omega_F$  is the flapping angular frequency, and  $K \in [0,1]$  is a smoothing parameter. The pitch motion has the same angular frequency and is defined by the following function:

$$\alpha_T(t) = \frac{a_T}{\tanh C_{\eta}} \tanh \left( C_{\eta} \sin \left( \omega_F t - \phi_T \right) \right) + \bar{\alpha}_T \tag{34}$$

where  $a_T$  denotes the pitch amplitude,  $\bar{\alpha}_T$  the incidence angle of the feather,  $C_\eta$  is the pitch smooth parameter, and  $\phi_T \in [0,2\pi[$  defines the phase difference of the pitch with respect to the flapping motion. Although the flapping pattern is defined by aerodynamic requirements, we vary the phase  $\phi_T$  and evaluate the kinematic ventilation parameter to gain insight into whether a given flapping pattern is favorable for opening the ventilation channels.

For a given flapping pattern, each point along a feather yields an optimal phase in terms of the kinematic ventilation parameter. Figure 6 shows the influence of the phase on the kinematic ventilation parameter. Figures 6a and 6b illustrate the flapping pattern and the obtained kinematic ventilation parameter for a pitch in phase with the flapping motion, i.e.,  $\phi_T = 0^{\circ}$ . Note that the parameter is positive during the first half of the stroke.

On the other hand, Figures 6c and 6d illustrate the phase of  $\phi_T = 120^{\circ}$ . Note that the kinematic ventilation parameter is positive for most of the cycle, with negative values occurring slightly before the stroke reversal. Parameters other than the phase, such as the pitch amplitude, can also be adjusted to increase the duration; however, this is a subject of analysis from other disciplines.

The flapping motion is imposed on each feather by prescribing both the position and orientation of the attachment node. The position of node A from the *i*th feather is prescribed in terms of the flapping motion as:

$$\mathbf{r}_{1,A}^{(i)}(t) = \mathbf{T}_{\alpha_F}^{\top}(t)_{\mathscr{B}_1} \mathbf{r}_P^{(i)},$$
 (35)

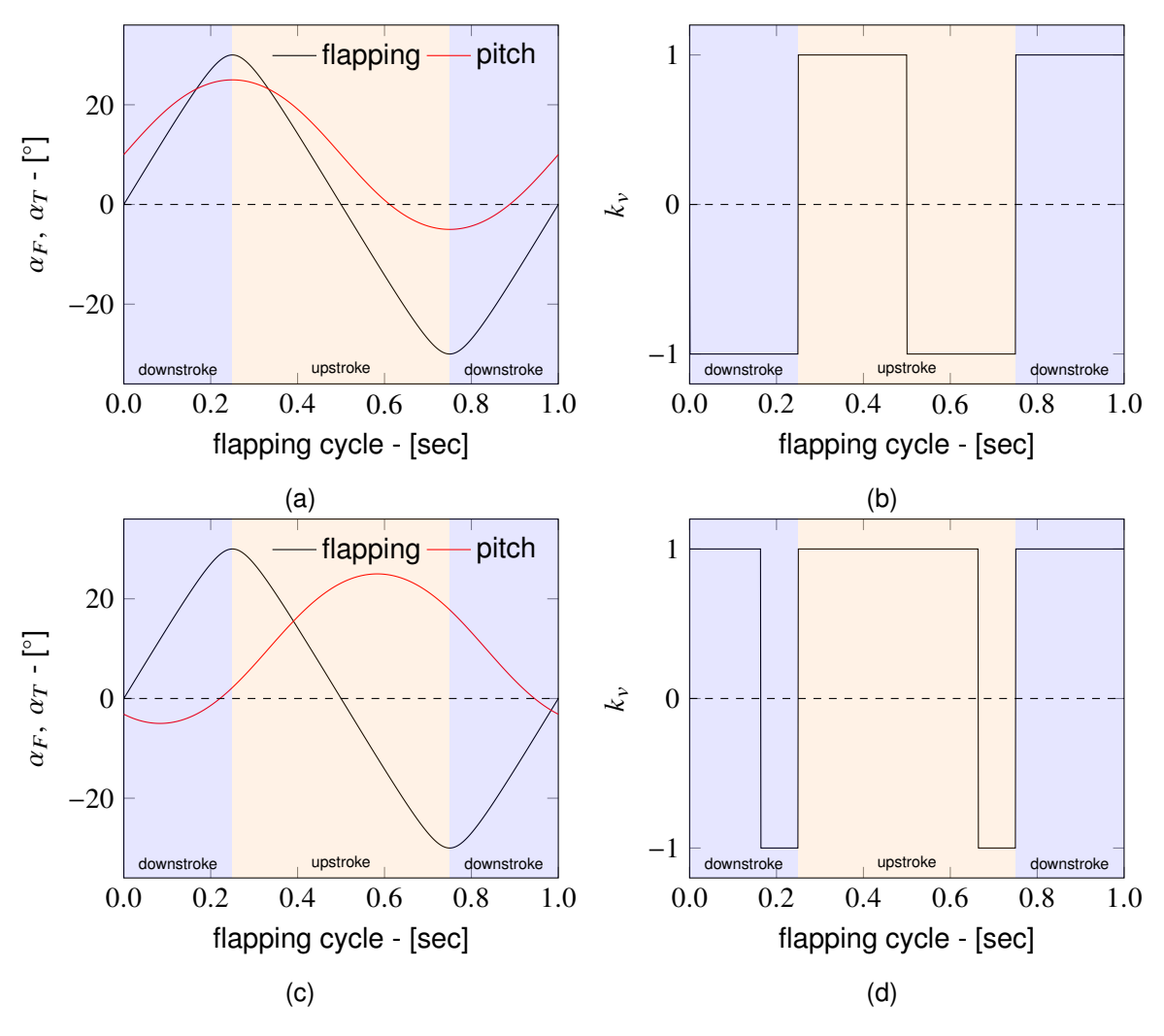


Figure 6 – Flapping pattern and the kinematic ventilation parameter considering a point at  $e_y = 0.2$ m,  $l_p = 0.3$ m. (a) and (b) are obtained considering a phase of  $\phi_T = 0^\circ$ , and (c) and (d) for  $\phi_T = 120^\circ$ .

and the slopes corresponding to the columns of the transformation matrix:

$$\left[ \frac{\partial \boldsymbol{r}_{1,A}^{(i)}(t)}{\partial x}^{\top} \quad \frac{\partial \boldsymbol{r}_{1,A}^{(i)}(t)}{\partial y}^{\top} \quad \frac{\partial \boldsymbol{r}_{1,A}^{(i)}(t)}{\partial z}^{\top} \right] = \boldsymbol{T}_{\alpha_F}^{\top}(t) \boldsymbol{T}_{\alpha_T}^{\top}(t) \boldsymbol{T}_{\alpha_G}^{\top}(t).$$
(36)

#### 5.5 Contact Monitor

The points of the contact surfaces are monitored using the closest point projection [19, p.114]. The upper-surface of the distal feather is denoted as the contactor surface  $\Gamma_c^{(2)}$ , whereas the lower-surface of the proximal feather is the target surface  $\Gamma_c^{(1)}$ . For a point i located at  $\boldsymbol{r}_i^{(2)} \in \Gamma_c^{(2)}$ , the minimum distance from the target surface  $\boldsymbol{r}^{(1)} \in \Gamma_c^{(1)}$  is obtained by solving

$$\mathbf{x}_{c}^{(1)}\left(\mathbf{x}_{i}^{(2)}\right) = \underset{\mathbf{x}^{(1)} \in \Gamma_{c}^{(1)}}{\arg\min} \|\mathbf{r}^{(2)}(\mathbf{x}_{i}^{(2)}) - \mathbf{r}^{(1)}(\mathbf{x}^{(1)})\|.$$
(37)

The gap is the projection from the points relative position to the normal direction from the target surface, obtained according to the following equation [20]:

$$g_{i}\left(\mathbf{r}^{(1)}\left(\mathbf{x}_{c}^{(1)}\left(\mathbf{x}_{i}^{(2)}\right)\right),\mathbf{r}^{(2)}\left(\mathbf{x}^{(2)}\right)\right) = \left(\mathbf{r}^{(2)}\left(\mathbf{x}^{(2)}\right) - \mathbf{r}^{(1)}\left(\mathbf{x}_{c}^{(1)}\left(\mathbf{x}^{(2)}\right)\right)\right)^{\mathsf{T}}\mathbf{n}^{(1)},\tag{38}$$

where  $\mathbf{n}^{(1)}$  denotes the unit vector normal to the target surface at  $\mathbf{x}_c^{(1)}$ . Thus, if the set of points  $\mathbf{x}_i^{(2)} \in \Gamma_c^{(2)}$ ,  $i = 1, \dots, m$ , are monitored, the following gap vector is defined:

$$g_{n} = \begin{cases} g_{1}\left(\mathbf{r}^{(1)}\left(\mathbf{x}_{c}^{(1)}\left(\mathbf{x}_{1}^{(2)}\right)\right), \mathbf{r}^{(2)}\left(\mathbf{x}_{1}^{(2)}\right)\right) \\ g_{2}\left(\mathbf{r}^{(1)}\left(\mathbf{x}_{c}^{(1)}\left(\mathbf{x}_{2}^{(2)}\right)\right), \mathbf{r}^{(2)}\left(\mathbf{x}_{2}^{(2)}\right)\right) \\ \vdots \\ g_{m}\left(\mathbf{r}^{(1)}\left(\mathbf{x}_{c}^{(1)}\left(\mathbf{x}_{m}^{(1)}\right)\right), \mathbf{r}^{(2)}\left(\mathbf{x}_{m}^{(2)}\right)\right) \end{cases}.$$
(39)

The impenetrability condition states that  $g_i \ge 0$ , i = 1,...,m [20, p.380], implying that the contactor point cannot cross the target surface. However, the continuous contact framework allows for a local indentation in the contact region by simultaneously including a set of opposing forces on each point [21]. This model requires accurate estimates of the contact-time to avoid unrealistic indentation that results in excessive contact forces [22].

#### 5.6 Event Detection

The event detection procedure consists of monitoring the signal from Equation 39. Whenever the sign of any component of  $g_n$  changes, an event occurs, which can be points contacting or separating. The following expression is evaluated for every component of the gap vector.

$$g_i(t_k)g_i(t_{k+1}) < 0. (40)$$

After the event is detected, two instants are identified: the pre-event  $^-t$ , and the post-event  $^+t$ . In between these instants occurs the event at  $t_c$ . The solution obtained at  $^+t$  is inaccurate, as the system dynamic changed after  $t_c$ . Thus, the following procedure is used to obtain  $t_c$ .

Consider the event detected for the ith component of Equation (39). The approach velocity,  $\dot{g}_i$ , between the contactor and the target points is obtained by differentiating Equation 38 with respect to time t. Assuming the approach velocity approximately constant between  $^-t$  and  $t_c$ , the following equation is obtained by a first order expansion of  $g_i$  at  $^-t$ :

$$h_e = -\frac{g_i \left( {^-}t \right)}{\dot{g}_i \left( {^-}t \right)},\tag{41}$$

where  $h_e$  is the estimated time-step required for the system to intercept  $g_i = 0$ .

Thus, after an event is detected at  $^+t$ , the system configuration is rewind to  $^-t$ . Then a single integration step with  $h_e$  is performed.

# 5.7 Contact Forces

The contact force is applied to the nodes as generalized forces [23]. For each component of Equation (39), a corresponding contact force is computed in terms of the penetration amount and the material properties as:

$$f_c = \begin{cases} -K_c g_i \boldsymbol{n}^{(1)}, & \text{if } g_i < 0, \\ \boldsymbol{0}, & \text{if } g_i \ge 0. \end{cases}$$

$$(42)$$

where  $K_c$  is the local contact stiffness. The generalized forces acting on the proximal and distal feathers are, respectively:

$$\boldsymbol{f}_{c}^{(1)} = -\boldsymbol{S}^{(1)}(\boldsymbol{\xi}_{c}, \eta_{c}, \boldsymbol{\zeta}_{c})^{\mathsf{T}} \boldsymbol{f}_{c}, \tag{43}$$

$$f_c^{(2)} = S^{(2)}(\xi_r, \eta_r, \zeta_r)^{\mathsf{T}} f_c.$$
 (44)

## 5.8 Equation of Motion

The equation of motion for each nodal coordinate of the *i*th feather is obtained by applying the Euler-Lagrange equation to the Lagrangian functional  $\mathcal{L} = \mathcal{T} - \mathcal{U}_e$  [24]. The result is the following set of second-order differential equations that model the dynamics of the flexible feather model:

$$M^{(i)}\ddot{e}^{(i)}(t) = f^{(i)}$$
 (45)

 $f^{(i)} = f_e^{(i)} + f_d^{(i)} + f_c^{(i)}$ , with  $f_e^{(i)}$  being the vector of nodal elastic forces obtained in Equation 31,  $f_d^{(i)}$  the vector of damping forces, and  $f_c^{(i)}$  the contact nodal forces from Equation 43 or 44. This system of equations is split into two sets, representing the prescribed coordinates and free coordinates denoted by the subscript p and f, respectively:

$$\begin{bmatrix}
\mathbf{M}_{pp}^{(i)} & \mathbf{M}_{pf}^{(i)} \\
\mathbf{M}_{fp}^{(i)} & \mathbf{M}_{ff}^{(i)}
\end{bmatrix} \begin{pmatrix} \ddot{\mathbf{e}}_{p}^{(i)} \\ \ddot{\mathbf{e}}_{f}^{(i)} \end{pmatrix} = \begin{pmatrix} \mathbf{f}_{p}^{(i)} + \mathbf{f}_{Reaction} \\ \mathbf{f}_{f}^{(i)} \end{pmatrix}.$$
(46)

Since the acceleration of the prescribed nodes is known due to the imposed flapping motion, the remaining f variables are solved by the following equation

$$\boldsymbol{M}_{ff}^{(i)}\ddot{\boldsymbol{e}}_{f}^{(i)}(t) + \boldsymbol{M}_{fp}^{(i)}\ddot{\boldsymbol{e}}_{p}^{(i)}(t) = \boldsymbol{f}_{f}^{(i)}(\boldsymbol{e}^{(i)}(t))$$
(47)

## 6. Results

The feathers consist of two identical rectangular beams that overlap and are subjected to an imposed flapping pattern. The equation of motion is solved using the implicit generalized- $\alpha$  method [26]. It is unconditionally stable and allows for the use of large time steps by filtering high-frequency modes associated with the finite element mesh [27]. The value and description of the material and algorithmic parameters are given in Table 2.

Table 2 – Parameters employed for evaluating the ventilation dynamics.

usage	symbol	description	value	unit
	ho	specific mass	2810	$kg / m^3$
material properties	$\boldsymbol{E}$	Young modulus	71.7	GPa
	ν	Poisson coefficient	0.0	-
	$l_p$	attachment position	0.2	m
	$l_f$	feather length	0.3	m
geometry	w	feather width	25	mm
	h	feather height	0.5	mm
	$w_o$	feather overlap	0.15	
	$a_F$	flapping amplitude	30	degrees
	$a_T$	pitch amplitude	15	degrees
flapping pattern	$ar{lpha}_T$	mean pitch	10	degrees
napping pattern	$\omega_F$	flapping angular frequency	$4\pi$	rad/s
	K	smoothing parameters	0.95	-
	$C_{\eta}$	pitch smooth	0.4	-
contact $K_c$		contact stiffness	20	N/m
mesh	n	number of elements	10	-
algorithic parameters	h	time step	0.01	sec
algorithic parameters	$ ho_{\infty}$	spectral radius	8.0	-

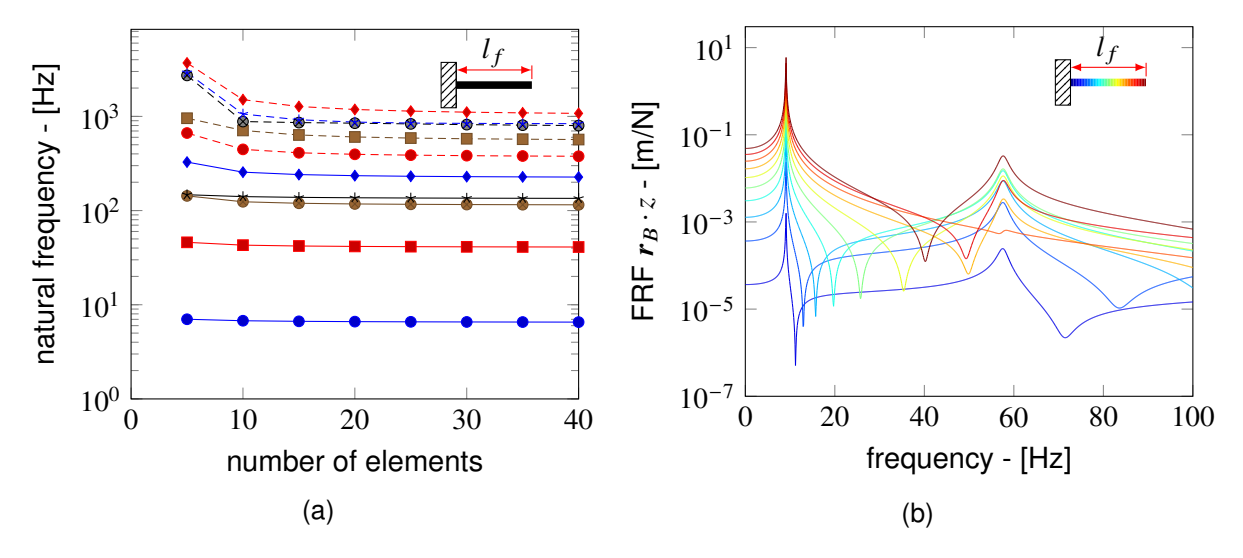


Figure 7 – Modal analysis from the feather structure. (a) illustrate the convergence of the 10 first natural frequencies of the mesh and an inset illustrating the boundary condition. (b) shows the frequency response function of the vertical displacement of nodes along the feather.

#### 6.1 Flexible Feathers

The trajectories of the flexible feathers without the contact model have been obtained. Figure 8 shows the position of the tips of the proximal and distal feathers. During the first second of the flapping cycle, the flapping pattern is modulated using a smoothstep function. After this period, the system oscillates according to the imposed motion. The large difference in the x coordinate between feathers in Figure 8a correspond to the fact that the distal feather,  $S_2$ , is attached far from the flapping joint. Part of the difference observed in Figure 8c is attributed to the increased amplitude of motion. The other part is due to the increased inertial loads.

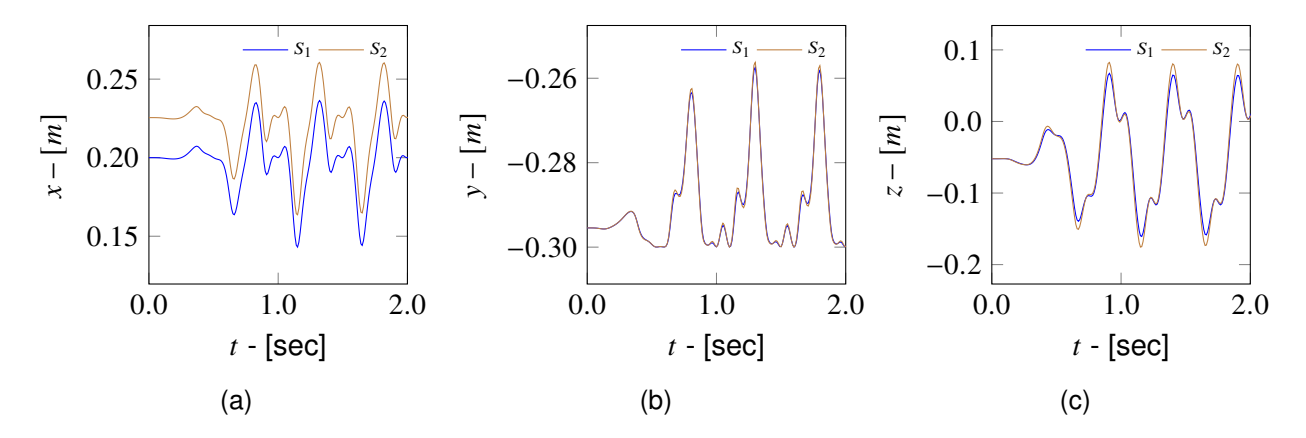


Figure 8 – Trajectories of the tip of the isolated flexible feathers model.

The gap between the tip of the distal feather and the closest projection on the surface of the proximal feather is presented in Figure 9. The positive gap indicates that the tip of the distal feather is below the surface of the proximal feather, while the negative values indicate that the tip is penetrating the surface of the proximal feather, thus violating the impenetrability condition. The gray region in the figure illustrates when the condition is violated. The continuous contact model is implemented to limit the physical inconsistency of the penetrating bodies.

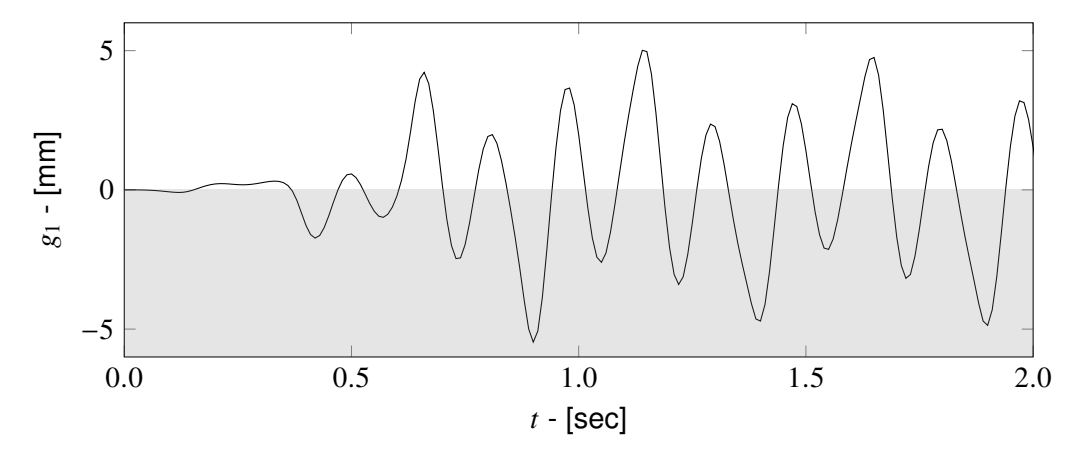


Figure 9 – Gap between the tip of the distal feather and the surface of the proximal feather without considering the contact.

## 6.2 Contact Feathers

The contact between feathers is modeled using the continuous contact formulation presented in Section 5.7 The position of the tip of each feather with respect to the time is presented in Figure 10. We also show the configuration of the system in the space at two instants of time, during the upstroke, as shown in Figure 11a, and during the downstroke, shown in Figure 11b.

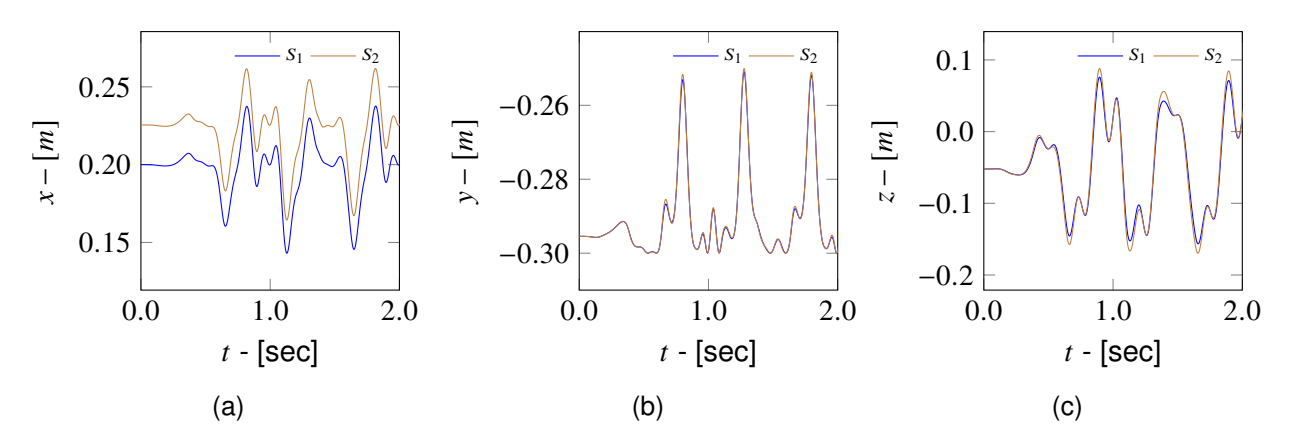


Figure 10 – Trajectories of the tip using the contact model.

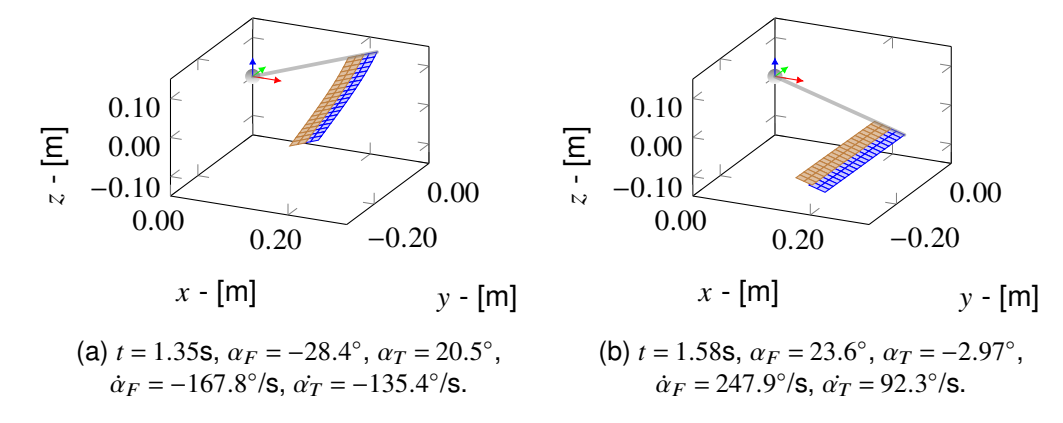


Figure 11 – Snapshots of the feathers configuration during the flapping stroke. (a) and (b) shows the structure configuration during the upstroke and downstroke, respectively.

The gap between feathers with contact is presented in Figure 12 by the solid black line. Compared with the gap obtained by the model without contact, illustrated by the dashed red line, the continuous contact model reduces the amount of penetration. However, the value of contact coefficient requires further tuning

to provide an accurate measurement of the geometry of the ventilation channels during the flapping cycle. The model in [21] introduces a damping coefficient that depends on the velocity before impact and the coefficient of restitution.

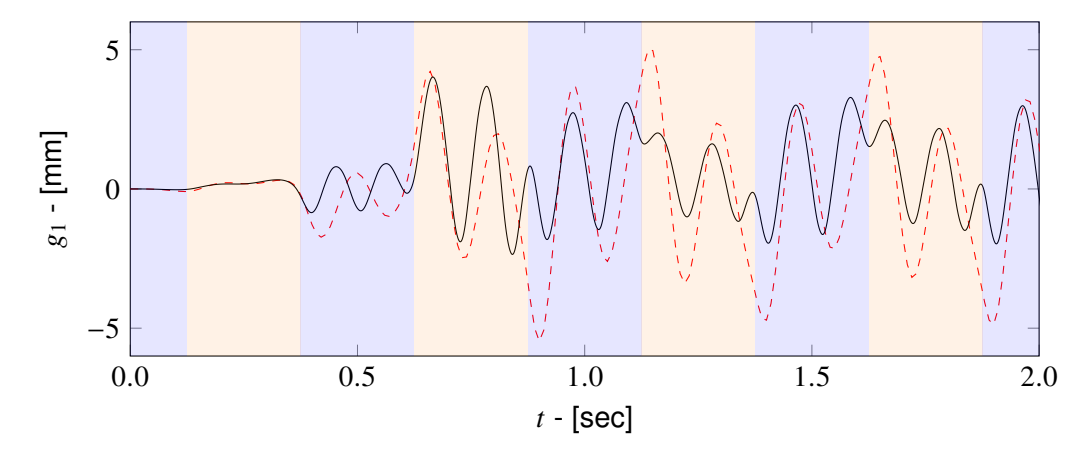


Figure 12 – Gap between the tip of the distal feather and the surface of the proximal feather using the continuous contact model.

The geometry of the ventilation channels is measured by positioning an observer rotating solidary with the feather and pointing to the  $_{\mathscr{B}_3}y$  direction. Then, the deflection of each feather can be visualized in the  $_{\mathscr{B}_3}x_{\mathscr{B}_3}z$  plane. Figure 13 shows the side of the distal feather and the projection of the proximal feather along the local coordinate system. The open and closed ventilation channels are presented in Figures 13b and 13a, respectively.

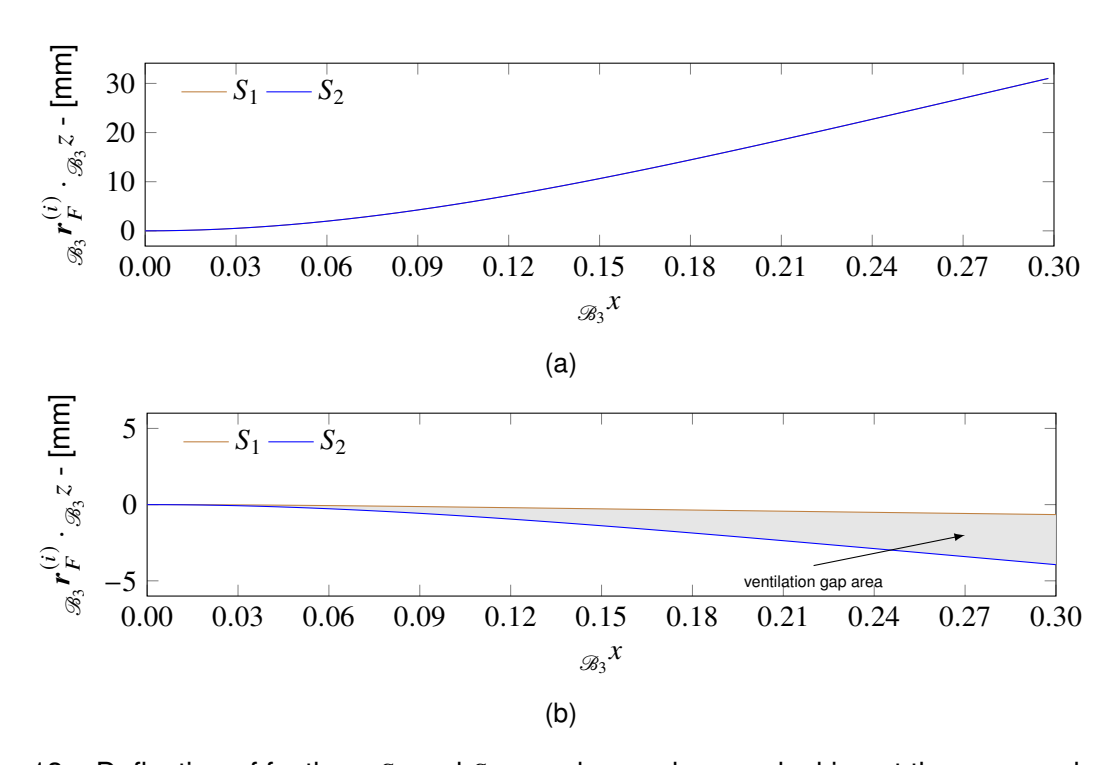


Figure 13 – Deflection of feathers  $S_1$  and  $S_2$  seen by an observer looking at the  $g_3 x g_3 z$  plane. (a) illustrate the closed channel between each feather and (b) the channel open.

The area between the curves in Figure 13 gives a measure of the geometry of the ventilation channels. For each instant of time, the absolute difference of the areas computed for each feather is presented in Figure 14. The negative values correspond to when the distal feather penetrates the surface of the proximal feather.

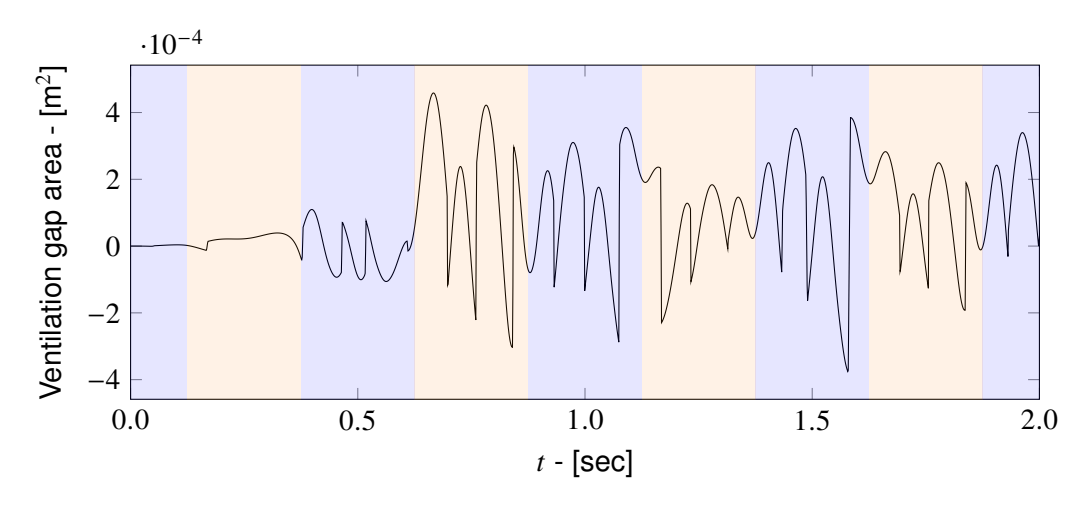


Figure 14 – Area of ventilation across the feathers. The areas in blue represent the downstroke whereas the areas in orange represent the upstroke.

## 7. Conclusion

The purpose of this work is to investigate the mechanism of formation of ventilation gaps observed during flight of feathered birds. This ventilation strategy is expected to increase the overall efficiency of a feathered flapping-wing UAV. The upstroke phase of the flapping cycle contributes negatively to the generation of thrust and lift forces. Therefore, by reducing the influence of this phase, an increase in the mean lift and thrust should be achieved.

The flapping motion induces an inertial load that increases for feathers positioned further from the flapping joint. In a feather pair, the increased load on the distal feather is balanced by a corresponding increase in its deflection, thus separating it from the proximal feather and allowing air to easily flow through this created gap. This effect is restricted during the downstroke because the overlap stops the distal feather from deflecting more than the proximal feather.

A kinematic analysis shows that modulating the phase of the pitch motion is an effective way to tailor the inertial loads so that the ventilation gaps open and close during the appropriate strokes. However, the kinematic model is limited because it essentially ignores the deformation on each feather. Therefore, a dynamic analysis is required to obtain and measure the desired ventilation gaps.

The Absolute Nodal Coordinate Formulation is used to model feather flexibility under an imposed flapping pattern. We monitor the gap between the distal feather and the proximal feather surface as a measure of the ventilation effect. Our findings demonstrate that the flexible model captures the separation between the feathers during both the upstroke and the downstroke. However, the obtained negative gaps are physically inconsistent due to violation of the impenetrability condition.

To solve this issue, the approach consists of monitoring the gap function; when a negative value is first detected, the system is rewound to the previous configuration to obtain an accurate estimate of the contact and loss of contact instants. This procedure avoids computing unrealistically high values of penetration that degrades the stability of the numerical solver. After the instant of contact is detected, the contact forces are evaluated to obtain the response of the system. However, further studies are required to determine the contact stiffness and model the coefficient of restitution during the impact.

#### 8. Contact Author Email Address

Mailto: cavenaghi.silva@unesp.br

## 9. Copyright Statement

The authors confirm that they, and/or their company or organization, hold copyright on all of the original material included in this paper. The authors also confirm that they have obtained permission, from the copyright holder of any third party material included in this paper, to publish it as part of their paper. The authors confirm that they give permission, or have obtained permission from the copyright holder of this paper, for the publication and distribution of this paper as part of the ICAS proceedings or as individual off-prints from the proceedings.

## 10. Acknowledgement

The authors appreciate the support under grant numbers: 2023/04325-3 and 2022/03128-7 from the São Paulo Research Foundation (FAPESP). The second author thanks the National Council for Scientific and Technological Development (CNPq), grant number 314151/2021-4.

## References

- [1] Umberto Pesavento and Z. Jane Wang. Flapping Wing Flight Can Save Aerodynamic Power Compared to Steady Flight. *Physical Review Letters*, 103(11):118102, September 2009.
- [2] Tarah N. Sullivan, Michael Chon, Rajaprakash Ramachandramoorthy, Michael R. Roenbeck, Tzu-Tying Hung, Horacio D. Espinosa, and Marc A. Meyers. Reversible Attachment with Tailored Permeability: The Feather Vane and Bioinspired Designs. *Advanced Functional Materials*, 27(39):1702954, 2017.
- [3] Jing-Shan Zhao, Jiayue Zhang, Yuping Zhao, Zhaodong Zhang, and Pascal Godefroit. Shaking the wings and preening feathers with the beak help a bird to recover its ruffled feather vane. *Materials & Design*, 187:108410, February 2020.
- [4] Tarah N. Sullivan, Bin Wang, Horacio D. Espinosa, and Marc A. Meyers. Extreme lightweight structures: avian feathers and bones. *Materials Today*, 20(7):377–391, September 2017.
- [5] Eric Chang, Laura Y. Matloff, Amanda K. Stowers, and David Lentink. Soft biohybrid morphing wings with feathers underactuated by wrist and finger motion. *Science Robotics*, 5(38):eaay1246, January 2020. Publisher: American Association for the Advancement of Science.
- [6] Steven J. Portugal, Tatjana Y. Hubel, Johannes Fritz, Stefanie Heese, Daniela Trobe, Bernhard Voelkl, Stephen Hailes, Alan M. Wilson, and James R. Usherwood. Upwash exploitation and downwash avoidance by flap phasing in ibis formation flight. *Nature*, 505(7483):399–402, January 2014.
- [7] Hans Försching and Holger Hennings. Aeroelastic mysteries in avian flight. *CEAS Aeronautical Journal*, 3(2-4):135–143, December 2012.
- [8] S. A. Combes and T. L. Daniel. Into thin air: Contributions of aerodynamic and inertial-elastic forces to wing bending in the hawkmoth Manduca sexta. *The Journal of Experimental Biology*, 206(Pt 17):2999–3006, September 2003.
- [9] Andrew A. Biewener. Biomechanics of avian flight. Current Biology, 32(20):R1110-R1114, October 2022.
- [10] Ahmed A. Shabana. Computer Implementation of the Absolute Nodal Coordinate Formulation for Flexible Multibody Dynamics. *Nonlinear Dynamics*, 16(3):293–306, July 1998.
- [11] Refaat Y. Yakoub and Ahmed A. Shabana. Three Dimensional Absolute Nodal Coordinate Formulation for Beam Elements: Implementation and Applications. *Journal of Mechanical Design*, 123(4):614–621, May 2000.
- [12] Daniel García-Vallejo, Aki M. Mikkola, and José Luis Escalona. A new locking-free shear deformable finite element based on absolute nodal coordinates. *Nonlinear Dynamics*, 50(1):249–264, October 2007.
- [13] Grzegorz Orzechowski and Ahmed A. Shabana. Analysis of warping deformation modes using higher order ANCF beam element. *Journal of Sound and Vibration*, 363:428–445, February 2016.
- [14] Johannes Gerstmayr and Ahmed A. Shabana. Analysis of Thin Beams and Cables Using the Absolute Nodal Co-ordinate Formulation. *Nonlinear Dynamics*, 45(1):109–130, July 2006.
- [15] A. A. Shabana, H. A. Hussien, and J. L. Escalona. Application of the Absolute Nodal Coordinate Formulation to Large Rotation and Large Deformation Problems. *Journal of Mechanical Design*, 120(2):188–195, June 1998.
- [16] A. L. Schwab and J. P. Meijaard. Comparison of Three-Dimensional Flexible Beam Elements for Dynamic Analysis: Classical Finite Element Formulation and Absolute Nodal Coordinate Formulation. *Journal of Computational and Nonlinear Dynamics*, 5(011010), December 2009.
- [17] D. García-Vallejo, J. Mayo, J. L. Escalona, and J. Domínguez. Efficient Evaluation of the Elastic Forces and the Jacobian in the Absolute Nodal Coordinate Formulation. *Nonlinear Dynamics*, 35(4):313–329, March 2004.
- [18] Garcíd, D. a Vallejo, J. Valverde, and J. Domínguez. An Internal Damping Model for the Absolute Nodal Coordinate Formulation. *Nonlinear Dynamics*, 42(4):347–369, December 2005.
- [19] Tod A. Laursen. Computational Contact and Impact Mechanics. Springer, Berlin, Heidelberg, 2003.
- [20] Nam-Ho Kim. Introduction to Nonlinear Finite Element Analysis. Springer US, New York, NY, 2015.
- [21] Parviz E. Nikravesh and Mohammad Poursina. Determination of effective mass for continuous contact models in multibody dynamics. *Multibody System Dynamics*, 58(3):253–273, August 2023.
- [22] Paulo Flores and Jorge Ambrósio. On the contact detection for contact-impact analysis in multibody systems. *Multibody System Dynamics*, 24(1):103–122, June 2010.
- [23] Jussi T. Sopanen and Aki M. Mikkola. Description of Elastic Forces in Absolute Nodal Coordinate Formulation. *Nonlinear Dynamics*, 34(1):53–74, October 2003.

- [24] Herbert Goldstein. Classical mechanics. Addison Wesley, San Francisco, 2002.
- [25] J. R. Dormand and P. J. Prince. A family of embedded Runge-Kutta formulae. *Journal of Computational and Applied Mathematics*, 6(1):19–26, March 1980.
- [26] Martin Arnold and Olivier Brüls. Convergence of the generalized- $\alpha$  scheme for constrained mechanical systems. *Multibody System Dynamics*, 18(2):185–202, September 2007.
- [27] Michel Géradin and Alberto Cardona. *Flexible multibody dynamics: a finite element approach*. John Wiley, New York, 2001.